PAPER

Check for updates

Deposition of triazine-based graphitic carbon nitride *via* plasma-induced polymerisation of melamine†

Charlotte Ruhmlieb, [iD] *[a] Maria Taplick,[a] Matz Nissen, [iD] [b] Ivan Baev,[b] Christian Strelow,[a] Sebastian Hentschel,[a] Marcel Dohrmann,[a] Michael Martins, [iD] [b] Tobias Kipp [iD] [a] and Alf Mews [iD] [a]

We present a novel plasma-assisted approach to deposit crystalline triazine-based graphitic carbon nitride directly onto solid substrates by fast and specific polymerisation of 2,4,6-triamino-1,3,5-triazine (melamine) in a pulsed rf plasma. We extensively investigate the molecular structure of the melamine precursor by single-crystal diffraction and bond-energy calculations. Moreover, thermogravimetric analysis is conducted to characterise the vaporisation behaviour of melamine. To get insights into the fragmentation of the monomer upon electron impact in the plasma, *in situ* optical emission spectroscopy is performed. Accurate assignment of the deposition product and its identification as pure triazine-based graphitic carbon nitride involve powder X-ray diffraction and an extensive study *via* X-ray photoelectron spectroscopy, which excludes the presence of other carbon nitrides. A band gap of 2.1 eV is identified *via* photoluminescence spectroscopy. Applying a constant dc bias of -210 V relative to ground to the non-heated substrate yields selectivity and prevents the co-deposition of melamine. We identify millisecond plasma pulses and a low duty cycle to be crucial for gaining a sponge-like morphology of the product, which is beneficial for catalytic purposes. Finally, the deposited polymer is investigated in terms of its photocatalytic behaviour by water-splitting experiments.

Introduction

With respect to the diminishing availability of fossil fuels and massive emission of harmful greenhouse gases, the ecological production and consumption of non-fossil fuels is becoming increasingly important. Due to its extraordinarily high net calorific value[1] and its presence in atomically bound form in abundant chemical compounds, hydrogen gas is often called the energy source of the future.[2] Hence, great efforts are being made to find economic ways to produce hydrogen as energy-efficient as possible. One approach is the light-induced dissociation of water on the surface of photocatalysts. Triazine-based

[a]University of Hamburg, Institute of Physical Chemistry, Grindelallee 117, 20146 Hamburg, Germany. E-mail: charlotte.ruhmlieb@uni-hamburg.de

[b]University of Hamburg, Institute for Experimental Physics, Luruper Chaussee 149, 22761 Hamburg, Germany

† Electronic supplementary information (ESI) available: (1) Photograph of the reaction chamber, (2) plot of Maxwell–Boltzmann distribution, (3) TGA data of the deposited TGCN sample, (4) close-up photographs of bare wafer and the TGCN sample, (5) tilted-view SEM image of the TGCN film at the wafer edge, (6) EDX data of the TGCN sample, (7) FT-IR spectra of melamine and the TGCN sample, (8) SEM image of TGCN deposited in the continuous plasma mode and the corresponding X-ray diffractogram, (9) XRD data of melamine and TGCN samples deposited under different dc bias conditions. See DOI: 10.1039/d2ta00491g

graphitic carbon nitride (TGCN) is one of the most promising metal-free catalysts for various oxidation and reduction reactions, in particular for water splitting.[3–6]

TGCN is an organic semiconductor with the sum formula C_3N_4. Its structure can be described as a two-dimensional conjugated polymeric network in which aromatic triazine monomers are linked *via* bridging nitrogen atoms. Due to this stringent linkage pattern of the monomers, there are virtually no scalable preparation methods to date for precisely fabricating triazine-based graphitic carbon nitride. The material is exclusively composed of alternating covalently bonded sp^2-hybridised carbon and nitrogen atoms, forming a two-dimensional aromatic network, thus representing a structural analogue of graphene. Unlike graphene, however, TGCN features a direct band gap of 2.4 eV (single sheet) to 2.0 eV (stacked), which is due to the lone pair electrons of the nitrogen atoms.[7,8] As schematically shown in Fig. 1, TGCN formally consists of polycondensed 2,4,6-triamino-1,3,5-triazine ($C_3N_6H_6$) units, also known as melamine. The two-dimensional linkage occurs *via* the amine substituents by abstraction of ammonia, which inevitably results in the formation of (nucleophilic) pores of a size of approx. 5 Å.[9] The stacking of TGCN layers in the AB or ABC pattern occurs *via* van-der-Waals forces.[9]

While TGCN has been described in several theoretical studies,[10–12] just a very few publications explicitly report on its

9680 | *J. Mater. Chem. A*, 2022, **10**, 9680–9692

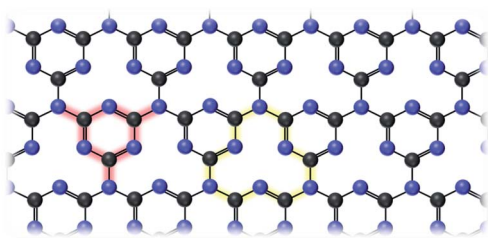This journal is © The Royal Society of Chemistry 2022

Fig. 1 Schematic illustration of the molecular structure of TGCN (carbon atoms in black, nitrogen atoms in blue). TGCN is composed of polycondensed melamine units (highlighted in red). The linkage *via* the substituents results in the formation of a two-dimensional network regularly interspersed with pores (highlighted in yellow).

synthesis. It should be noted that detailed analyses are required to clearly distinguish TGCN from other carbon nitrides, *e.g.*, from heptazine-based graphitic carbon nitride (HGCN) or poly(triazine) imide (PTI),[13] which can form under similar synthesis conditions. One popular technique for the production of graphitic carbon nitrides is the solvothermal synthesis. For this approach, various carbon and nitrogen precursors, such as dicyandiamide ($C_2H_4N_4$) or halogenated triazines, are mixed in an autoclave together with organic solvents, *e.g.*, benzene or cyclohexane.[14–17] The reaction takes place at high pressure when the mixture is heated to normally a few hundred degrees Celsius for several hours. The idea of using high pressure is in principle reasonable to produce TGCN, since TGCN is considered to be energetically less favoured than HGCN.[18] However, to the best of our knowledge, forming TGCN has not been achieved *via* solvothermal approaches so far.

One method that demonstrably led to the formation of TGCN is the ionothermal polycondensation, first described by Algara-Siller *et al.* in the year 2014 and modified by Noda *et al.* for the deposition of TGCN on SiO_x slides.[7,19] Briefly, a conglomerate of dicyandiamide and a eutectic salt mixture of LiBr and KBr is heated within a closed ampoule system following a specific temperature protocol. The overall heating procedure, with a maximum temperature of 600 °C, takes approx. 64 hours and leads to an opaque dark-brown film on glass.[19] The fact that TGCN is deposited directly on a substrate is of great advantage. In contrast to powders that need to form stable suspensions, deposited TGCN can be handled as a physical unit with distinct dimensions. Moreover, deposited films offer better processability, *e.g.*, for multilayer formation and contacting, for electronic device fabrication.

Chemical vapour deposition (CVD) techniques offer the possibility for the controllable and precise deposition of materials onto substrates. In fact, there are a few CVD approaches reported for the deposition of carbon nitrides from the gas phase.[20,21] The procedure by Kouvetakis *et al.* is based on the thermal decomposition of freshly prepared halogenated trimethylsilyl triazines at 400–500 °C and apparently leads to TGCN on solid substrates.[20] The need for elevated deposition temperatures represents a sensitive limitation for CVD, particularly in terms of possible substrate materials. The use of plasma as a reactive medium allows for significantly lower substrate temperatures.

Moreover, plasma-enhanced chemical vapour deposition (PECVD) tolerates the use of less complex precursors so that even conventional gases such as methane or ammonia can be used as carbon and nitrogen sources for carbon-nitride deposition.[22–25] Interestingly, carbon nitrides grown by PECVD often exhibit nanostructuring.[25] Thus, compared to a plane film, an increased surface area is created, which in turn can further increase the (photo)catalytic activity of the deposited material per nominal substrate area. However, the previously reported PECVD processes preferably lead to hydrogenated amorphous carbon-nitride structures, but not to the desired TGCN.

We report a novel plasma-based approach for the fast and direct deposition of nanostructured crystalline TGCN onto solid substrates under mild conditions using a home-built PECVD system. Unlike conventional (PE)CVD approaches, we do not use gaseous precursors but insert solid melamine as a monomer that is thermally evaporated inside the reaction chamber and release it into a pulsed plasma. In this way, the fundamental molecular structure of the later product is inherently existent already in the precursor. The monomers only have to be linked by activating the substituents with low-energy plasma pulses. Thus, we do not rely on the arbitrarily correct arrangement of carbon and nitrogen from decomposed methane and ammonia, but precisely polymerise melamine in the gas phase to form pure, crystalline TGCN. Firstly, we focus on the characterisation of the solid single-source precursor melamine, its crystal structure and thermal stability. Then we show how this precursor is thermally vapourised into a capacitively-coupled radio-frequency Ar/N_2 plasma. We present spectroscopic data to explore how the monomer molecules are activated or decomposed into reactive fragments by millisecond plasma pulses. The main part of the study describes the characterisation of the deposited TGCN films. Here, we present a detailed combined analysis of the deposited structure *via* X-ray diffraction, photoluminescence spectroscopy and X-ray photoelectron spectroscopy that clearly confirms the deposited product to be pure TGCN. Finally, we demonstrate the photocatalytic activity of the deposited material for water splitting.

Experimental

Chemicals

All chemicals were used without further purification. Melamine ($C_3H_6N_6$, Sigma Aldrich, ≥99%) was used as the precursor; argon (Ar, Westfalen, 5.0) and nitrogen (N_2, Westfalen, 5.0) functioned as carrier gases for the plasma-induced polymerisation. Heavy water (D_2O, ≥99.9%) was purchased from Sigma Aldrich.

Single-crystal fabrication of melamine

Single crystals of melamine were grown by preparing a critical solution of melamine in bidistilled water. For this, in a round-bottomed flask, 950 mg (7.5 mmol) melamine was dissolved under stirring at 700 rpm in 200 mL water and normal pressure at a temperature of 80–82 °C. Subsequently, the clear hot solution was filtered through a filtration paper (particle retention 8–12 μm) into 20 mL glass vials. After a few seconds,

This journal is © The Royal Society of Chemistry 2022

J. Mater. Chem. A, 2022, **10**, 9680–9692 | **9681**

colourless single crystals formed with a size of a few hundred micrometres.

Bond-energy calculations

DFT calculations were executed using the Gaussian 09W software.[26] With the commonly used hybrid-DFT-functional B3LYP and the triple-zeta Dunning basis set cc-PVTZ, binding energies of the melamine precursor were calculated. The energy criteria for the geometry optimisation of the aromatic fragments (bond dissociation of $C–NH_2$ and NH–H) were set to 10^{-6} Hartree. By default, four additional convergence criteria for optimisation were applied. The threshold of the maximum force component (0.450×10^{-3} Hartree/Bohr radius; 3.707×10^{-11} N), the root mean square force (0.300×10^{-3} Hartree/Bohr radius; 2.780×10^{-11} N) and for displacement the maximum step component (1.800×10^{-3} Bohr radius; 95.25×10^{-15} m) and root mean square step (1.200×10^{-3} Bohr radius; 63.50×10^{-15} m) were fixed. Fragments upon bond breaks within the aromatic ring were not optimised in geometry due to chemical and structural plausibility.

Thermogravimetric analysis

Thermogravimetric measurements were performed using a Netzsch STA 449 F3. For investigating the evaporation of melamine upon heating, 20.10 mg of melamine was heated at a rate of 10 °C min^{-1} up to 400 °C in an argon atmosphere at normal pressure. To investigate the thermal stability of the deposited structures, six wafer substrates covered with overall 13.20 mg product were heated up to 800 °C (5 °C min^{-1} rate) in an argon atmosphere at normal pressure. Afterwards, the blank wafers were heated identically for identification of the uplift.

Powder X-ray diffraction

All samples were investigated *via* powder X-ray diffraction with Cu Kα radiation (1.54439 Å) using an X'pert Pro MPD (Philips) in the 2θ range of 5 to 60°. For each measurement, the entire sample was placed on a substrate holder that was lowered in height by the thickness of the substrate. The data were processed using X'pert Pro software. The Sonneveld & Visser method was performed for background correction (segmentation: 20, curvature: 5).

Substrate preparation

Prime grade silicon wafers without an oxidised layer were purchased from Addison Engineering, Inc. San Jose, CA. The crystal orientation of the 625 μm thick n-type doped wafers was (100). Before usage, the wafers were sonicated in acetone for 15 min and were dried under nitrogen flow. For UV/Vis spectroscopy the TGCN was deposited on ITO-covered glass slides that were used without any additional cleaning.

Deposition procedure

Plasma-induced polymerisation was performed using a modified home-built setup as shown in the ESI in Fig. S1† and described in detail elsewhere.[27] The radio frequency of the

capacitively-coupled plasma was 27.12 MHz. Argon and nitrogen were used as carrier gases. Typically, 500 mg of melamine is placed in a molybdenum crucible on a resistance heating plate in vertical alignment with a biased micro clamp, holding the silicon wafer or ITO-covered glass slide face-down. For the synthesis, the bias of the substrate is set to −210 V relative to ground. The chamber pressure is adjusted to 5 mbar at an argon flow of 139 sccm and a nitrogen flow of 12 sccm. After two minutes of continuous plasma operation at 10 W plasma power, the plasma is switched to pulsed mode (5 ms on and 15 ms off, 25% duty cycle). Then, the precursor is heated with approx. 20 °C min^{-1} to 300 °C. After a particular reaction time, typically 10 min, the precursor heating is stopped. By the time the emission spectrum of the plasma indicates no further existence of precursor in the gas phase, the plasma is turned off. The substrate is removed at room temperature.

Optical emission spectroscopy

Optical emission spectroscopy was performed with a home-built setup positioned close to an optical quartz glass window of the plasma chamber. The setup consists of two lenses and a spectrograph (30 cm focal length, 300 gr per mm grating with 300 nm blaze wavelength) with a CCD camera (Andor iDus 420 OE) mounted on top of an optical breadboard. The light of the plasma from the sample region inside the chamber was transmitted through an optical quartz window of the reaction chamber and was collected from the first lens. The second lens focused the light on the entrance slit of the spectrograph. Tuning the grating to zeroth order and completely opening the slit allowed for direct imaging of the sample region and thus controlling the collection spot inside the chamber. For the spectroscopy, the slit was closed, and the grating was tuned to the first diffraction order. Spectra were taken continuously every 100 ms during the synthesis.

Scanning electron microscopy

All samples were investigated *via* scanning electron microscopy to visualise the morphology of the deposited structures using a Zeiss LEO 1550 with a beam energy of 2 kV at a chamber pressure of approx. 1×10^{-6} mbar. All samples were measured in the original state without any pre-treatment.

Energy-dispersive X-ray spectroscopy

For the determination of the elemental composition of some samples, energy-dispersive X-ray spectroscopy was conducted on a Zeiss EVO-Ma using 22 kV beam energy and a scan time of 180 s per measurement. All determined values for the sample composition are the average value of six individual measurements on different spots of the sample, respectively.

Photoluminescence spectroscopy

Photoluminescence spectroscopy of the samples was conducted by using a home-built confocal microscope. For the excitation of the samples, laser light of 403 nm wavelength (ALS, PiL040X) was used. The laser light was filtered by a laser line filter

(405 nm with 10 nm bandwidth) and was focused by an epiplan apochromat 150×/NA 0.95 objective (Zeiss). The collected light was filtered with a long pass filter (430 nm). An Acton SP2300i spectrograph (Princeton Instruments, 300 grid lines per mm, 500 nm blaze) and a Pixis 400B CCD (Princeton Instruments) were used to record emission spectra of the samples. The spectra were evaluated with the programs Lightfield (Princeton Instruments) and OriginPro 2018G.

Infrared spectroscopy

For further structural investigation of the deposited product, Fourier-transform infrared spectroscopy was performed using a Varian 660 IR spectrometer equipped with an attenuated total reflectance (ATR) unit. After measurement of the background, a product-coated silicon wafer was pressed on the ATR crystal and was measured in the range of 500–4000 cm^{-1}. Using the software Varian Resolution Pro, the background was subtracted, and the absorption spectrum was transformed into the transmittance spectrum. The same procedure was performed for the measurement of melamine, but with pressing melamine powder on the ATR crystal.

X-ray photoelectron spectroscopy

X-ray photoelectron spectroscopy was used to analyse the chemical bonding state of the samples *ex situ*. The spectrometer was the hemispherical electron analyser SES2002 from Scienta. The base pressure during spectra acquisition was better than 5×10^{-9} mbar. The samples were spot-welded to a metallic base plate. The total drain current induced by X-rays was monitored in parallel. No charge neutralisation was employed. The excitation source was a non-monochromatised water-cooled twin anode Mg/Al X-ray gun. It was operated under Mg Kα radiation ($h\nu = 1253.6$ eV) with 300 W X-ray power at 12.5 kV acceleration voltage. The calibration and linearity of the binding energy scale were confirmed by examining freshly sputter-cleaned Au(111) and Ir(111) crystals. With the selected scan parameters, the overall energy resolution was 1 eV, which was determined from the FWHM of the Au 4f lines. For referencing, complementary work-function measurements were performed by ultraviolet photoelectron spectroscopy with monochromatised He I radiation ($h\nu = 21.22$ eV) and the same analyser using the energy cut-off.

Elemental analysis

Four silicon wafers with a size of 2.5 × 1.5 cm were covered with TGCN by performing the presented plasma-based procedure, respectively. Under great mechanical effort, 0.8 mg product in total was removed from the substrates using a metal spatula and was directly weighed in a zinc crucible. The amounts of carbon, nitrogen and hydrogen were measured using the UNICUBE elementar analyser (Elementar) with a thermal conductivity detector (precision of <0.1%).

UV/Vis spectroscopy

For investigating the absorbance properties of the samples, TGCN was deposited on ITO-covered glass slides. UV/Vis spectra were recorded in the range of 300 nm to 800 nm using a UV/Vis spectrometer (Cary 5000, Agilent Technologies Inc.) equipped with an integrating sphere. For this, the bare substrate and the samples were positioned in the centre of the sphere, respectively, to eliminate any loss of light due to reflection and scattering. Finally, all absorptance values (*i.e.* fraction of light being absorbed) were calculated according to the literature.[28]

Water-splitting experiments

Mass spectra were recorded using a Pfeiffer PrismaPro QMG 250 M1 mounted in the XPS experimental chamber. The neutral gas is ionised by the spectrometer with a filament before the entrance to the quadrupole section. A 365 nm (FWHM = 9 nm) LED M365LP1 from Thorlabs was mounted outside the vacuum chamber, illuminating the sample through a window at a working distance of 42 cm. The calculated irradiance was about 15 mW cm^{-2}. The pressure inside the chamber during the measurements was around 1×10^{-8} mbar.

Results and discussion

Melamine as the monomeric precursor

Melamine is an aromatic heterocycle with the chemical formula $C_3N_6H_6$. The molecule can be described as a 1,3,5-triazine aromatic ring with three amine substituents at positions 2, 4 and 6. In the present work, melamine was used as the precursor for the deposition of TGCN. Basically, the idea is to thermally evaporate melamine and to selectively activate the molecule in the gas phase by plasma impact, *i.e.*, through collisions with energetic electrons within one plasma pulse. The aromatic ring shall be preserved, while the splitting of the N–H bonds or the complete abstraction of NH_2 substituents shall result in the formation of radical aromatic species. In the plasma off-state, these radicals shall then recombine to form TGCN on the substrate.

At first, melamine was investigated in detail regarding its molecular structure, thermal stability, and fragmentation behaviour. For this, single crystals of melamine were grown and analysed *via* X-ray diffraction (XRD) to determine the relative atomic positions and bond lengths. These data were then used to calculate the bond energies. Thermogravimetric analysis (TGA) of melamine was performed to estimate its thermal evaporation behaviour. Finally, the fragmentation of melamine upon plasma impact was investigated *via* optical emission spectroscopy (OES).

The X-ray diffraction analysis of melamine single crystals reveals that melamine crystallises in space group $P2_1/n$ with four melamine molecules in the monoclinic unit cell ($a = 7.24$ Å, $b = 7.46$ Å, $c = 10.12$ Å, $\alpha = 90.0°$, $\beta = 108°$, $\gamma = 90.0°$). The bond lengths between the aromatic sp^2-carbon atoms and the sp^2-nitrogen atoms vary between 1.339 Å and 1.354 Å, while the bond lengths between sp^2-carbon atoms and sp^3-nitrogen atoms of the amine groups are measured to be about 1.345 Å. All bonds between nitrogen atoms and hydrogen atoms in the NH_2 substituents are 0.880 Å in length.

From the atomic positions obtained from X-ray diffraction, binding energies were calculated using DFT to identify stable

This journal is © The Royal Society of Chemistry 2022

J. Mater. Chem. A, 2022, **10**, 9680–9692 | **9683**

and fragile sites of the molecule. As depicted in Fig. 2(a), the energies of the N–H bonds (4.92 eV) and C–NH$_2$ bonds (4.86 eV) are significantly weaker than the bonds within the aromatic ring. The bond strength between sp^2-carbon and sp^2-nitrogen is about 6.46 eV, while Diels–Alder type fragmentation of the melamine molecule is associated with an energy of 10.3 eV. Hence, in first approximation, it can be deduced that the pre-formed binding motif of the triazine ring is likely to be preserved at a sufficiently low energy input. In fact, as an organic solid, melamine shows a relatively high thermal stability.

TGA of melamine was conducted by monitoring the weight loss of melamine powder upon heating under an argon atmosphere at normal pressure. The resulting TG curve is shown in Fig. 2(b). From room temperature up to 276 °C the weight of the melamine sample remains constant before a rapid decrease of the weight is displayed. At a temperature of 377 °C the curve flattens abruptly. The residual amount at 400 °C is 15.7 w%. The TGA results indicate that melamine starts to sublimate as an intact molecule at *ca.* 276 °C, confirming the data from the literature.[29] Thermal decomposition in this temperature interval can be excluded since there are no steps visible in the TG or DTG curve. Above 377 °C, the weight loss is decelerated since melamine undergoes condensation reactions under the release of ammonia forming involatile compounds.[30] Since

melamine sublimates at normal pressure, as proven by TGA, it can be assumed that melamine also evaporates undecomposed at lower pressure. Hence, when the powder is heated to 300 °C at 5 mbar within the PECVD chamber, as reported here, melamine firstly enters the plasma as an intact molecule.

The rf plasma is used as a non-thermal activation and reaction medium and its reactivity can be attributed to the oscillating electrons which collide with the precursor molecules in the gas phase. Depending on the kinetic energy of the colliding electrons, *i.e.*, the electron temperature T_e, and the number of collisions, processes like conversion, activation, ionisation, or fragmentation of the precursor can occur. Since radiative recombination of electrons with other species in the plasma can lead to intense UV radiation, also photo-induced reactions of the precursor or precursor species must be considered. The optical light emission of the plasma can be utilised to identify atomic and molecular species that are formed in the gas phase during the synthesis. For this, the overall emitted light of the plasma is collected and spectrally analysed. The measured emission lines can be associated with known atomic or molecular species. Optical emission spectroscopy represents a non-invasive remote technique to investigate plasma processes *in situ*.

We performed OES to check whether the chosen plasma conditions were sufficient to activate melamine. For this, the emission spectrum of pure argon plasma in the spectral range of 280 nm to 500 nm at 5 mbar chamber pressure and 10 W input power was measured. Then, the same experiment was repeated during additional evaporation of melamine. For assignability of possible nitrogen signals upon melamine fragmentation, pure argon plasma was used instead of the argon–nitrogen mixture as for the actual TGCN deposition. Like in the TGCN fabrication, the plasma was maintained in pulsed mode. The emission spectra of the pure argon plasma and the argon plasma at the same position during the evaporation of melamine are presented in Fig. 2(c). The pure argon spectrum shows a broad signal with peaks at 305.8 nm and 308.0 nm. These peaks can be assigned to OH$^+$ [31] and OH,[32] respectively, which is due to residual moisture. Additional signals appear when melamine enters the plasma. According to the literature, the distinct signals at 327.4, 334.8 and 335.6 nm can be unambiguously assigned to NH species.[32–35] The broader signal with local maxima at 355.3, 356.4, and 356.9 nm can be correlated with N$_2$.[36] The most intense signal can be observed between 383.8 nm and 386.8 nm, corresponding to cyanide (CN).[37–39] The peaks at 390.0 nm, 391.4 nm and 393.3 nm can be assigned to CH species,[40] while the signal at 391.4 nm could also be N$_2$$^+$.[41] Finally, the prominent multiplet with peaks at 412.1 nm, 413.8 nm, 414.3 nm, 415.2 nm, 416.8 nm, 418.4 nm and 420.3 nm is known as the CN violet band.[42]

The OES spectrum in Fig. 2(c) suggests a dominance of the CN species over the NH species which should be perceived with care, since different absorption and emission cross-sections of both species must be considered.[43] Qualitatively, the strong CN and CH signals confirm the sublimation of individual melamine molecules into the plasma and the distinct NH signals might result from the release of the amine groups. Since the NH
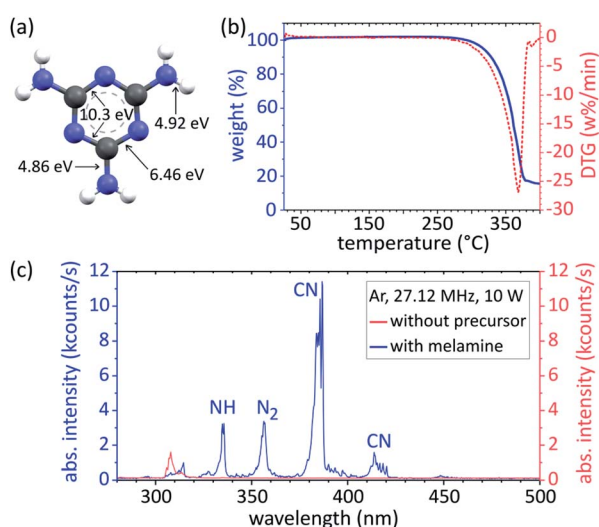

Fig. 2 (a) Ball-and-stick illustration of melamine with indication of the calculated binding energies. The bonds between the sp^2-hybridised aromatic carbon and nitrogen atoms are calculated to be *ca.* 6.5 eV in energy, which is much stronger than the bonds between sp^2-C and sp^3-N or sp^3-N and H. (b) Weight loss of melamine *versus* temperature at normal pressure with first deviation (DTG, red dotted line) of the TG curve (blue solid line). The one-step decrease indicates sublimation of melamine at a temperature of *ca.* 280 °C. (c) Optical emission spectrum of pure argon plasma (27.12 MHz, 10 W input power) at 5.0 mbar pressure (red, signals: 305.8, 308.0, 313.5 nm are assigned to OH species) and spectrum at the same position of the plasma during the sublimation of melamine (blue, signals: 334.8/335.6 nm are assigned to NH species, multipl. around 356.4 nm correlates with N$_2$, multipl. around 385.6 nm and multipl. around 416.8 nm are assigned to CN species).

9684 | *J. Mater. Chem. A*, 2022, **10**, 9680–9692

This journal is © The Royal Society of Chemistry 2022

signals are typically also observable in ammonia plasmas, fragmented NH_3 could also contribute to the NH signals. However, potential NH_3 most likely does not originate from polycondensation of the heated melamine, since no clear hydrogen signal, e.g., the H_β line at 485 nm,[44] is visible.

The appearance of additional signals during the evaporation of melamine in argon plasma reveals that even mild reaction conditions (5 mbar, 10 W input power) are sufficient to fragment thermally evaporated melamine molecules at least partially. The exact degree of fragmentation or the absolute amount of the respective fragments is not known since this is not an absolute-calibrated OES. Assuming that the electron energy distribution function (EEDF) of the used plasma can be described as a Maxwell–Boltzmann distribution and taking the average electron temperature T_e of 3.2 eV into consideration, as it was experimentally determined via the Boltzmann-plot technique,[45,46] it is very likely that only a small fraction of the melamine molecules are explicitly fragmented, as visible particularly from the CH and CN signals in the spectrum. Only a few high-energy electrons (fraction of electrons with >6.4 eV temperature is 26%, see Fig. S2†) might cause this strong fragmentation, while most of the electrons (fraction of electrons with <6.4 eV is 74%) contribute to the activation of melamine leading to soft fragmentation of the non-aromatic substituents. Hence, the majority of the precursor molecules is most likely unaffected, excited without further ionisation, or activated by abstraction of NH and/or H to undergo further reaction to form TGCN on the substrate. It has to be noted that volatile species such as NH_x, CH_x or CN require substrate temperatures of several hundred degrees Celsius to react on a substrate surface.[47,48] Thus, since the substrate is not actively heated, small volatile species that occurred from fragmentation of melamine play a less important role in the deposition of TGCN than the less volatile radical triazine species generated by abstraction or fragmentation of the amine substituents. The emission of these large aromatic species is to be expected in the higher energy UV range, which is not covered here.[49] In situ FT-IR spectroscopy of the plasma might be helpful to identify these bigger molecular intermediates. Overall, mainly based on the NH signals in the emission spectrum, it can be concluded that melamine is activated by fragmentation or abstraction of the amine groups and part of the melamine molecules is completely decomposed.

TGCN via plasma-induced polymerisation

For the deposition of TGCN on silicon wafers and ITO-covered glass slides, a melamine-filled molybdenum crucible is placed on a hot plate that is also the grounded electrode of the capacitively-coupled plasma (CCP) setup. Between the upper electrode and the hotplate, a metallic micro clamp holds the 1.0×1.5 cm large substrate face down in vertical distance to the precursor reservoir. By contacting the substrate-holding clamp, a dc bias of -210 V relative to ground is applied to the substrate. At 5 mbar chamber pressure the melamine powder is slowly heated to 300 °C while the Ar/N_2 plasma is pulsed 5 ms on and 15 ms off (25% duty cycle). After 10 min deposition time the

procedure is terminated by stopping the precursor heating. As a result, the substrate is homogeneously covered with a brownish-silvery coating, similar to that described for TGCN in the literature.[19] As proven by TGA measurements of the sample (see Fig. S3†), the product is thermally very robust. Other than polymeric HGCN,[50–52] the deposited material is still stable at 800 °C. The film is characterised by a noticeably matt appearance (see Fig. S4†) that already indicates a certain roughness. To investigate the topology of the sample in detail, scanning electron microscopy (SEM) was performed. A representative SEM image is shown in Fig. 3(a). The data not only confirm the presumed considerable roughness of the deposited film, but also reveal that the 4 μm thick layer, as determined via cross-sectional SEM images, consists of nanoscopic, mostly two-dimensional structures. Further SEM images (see Fig. S5†) show that the film is homogeneous and equally structured even to the outermost edge of the substrate, thanks to the gas-phase based methodology. Interestingly, the sample did not show any charging effects or damage during scanning with the electron beam, as it might be expected for insulating, at least amorphous, organic materials.[53] This implies a certain electrical conductivity of the deposited structure as it can be expected for a semiconductor material.

To determine whether the deposited product can be described as a type of graphitic carbon nitride in general, structural analysis of the sample was done at first by conducting powder X-ray diffraction (XRD) of the covered substrate. The
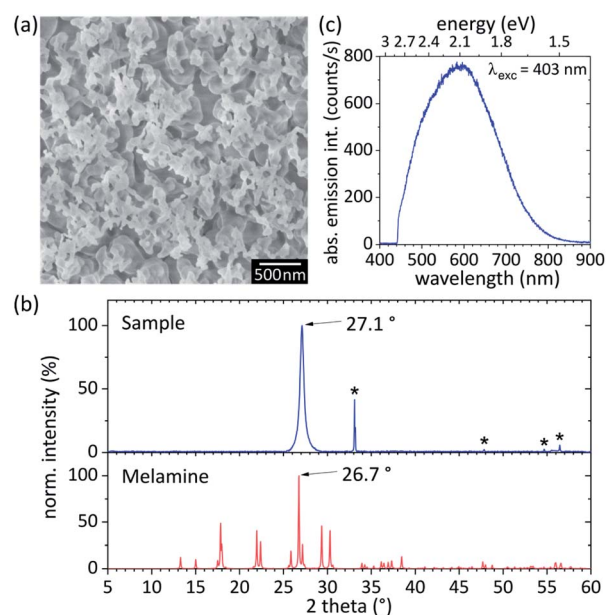

Fig. 3 (a) Scanning electron microscopy image (top view) of the deposited structures. The flake-like morphology creates a porous layer, that does not show any strong charging in the electron beam of the electron microscope. (b) Normalised powder X-ray diffraction data of the sample compared to the XRD pattern of melamine (* = wafer). (c) Photoluminescence spectrum of the sample upon optical excitation with 403 nm laser light (405 nm laser-light filter and 430 nm long-pass filter). The maximum of the broad emission signal is at approx. 591 nm (2.1 eV).

This journal is © The Royal Society of Chemistry 2022

J. Mater. Chem. A, 2022, **10**, 9680–9692 | **9685**

recorded diffractogram, shown in Fig. 3(b), is characterised by a very low background signal and features only one reflection at 27.1°. Using Bragg's equation, this reflection equals a d-spacing of 0.33 nm and thus can be assigned to the (002) plane originating from the periodic stacking of graphitic layers.[54] A reflection at 13.0° which is often related in the literature to the intralayer d-spacing[54] (hole-to-hole distance of the nitride pores) of g-C$_3$N$_4$ was not observed here (even without baseline correction) which is a strong indication for the absence of melon,[55] PTI[13] and HGCN.[56] However, it cannot be excluded that the small lateral size of the single-crystalline flakes causes vanishing of a reflection at 13.0°. Hence, from the XRD data it can be deduced that the presented plasma-based approach leads at first to the formation of a graphitic material. Moreover, the XRD patterns of the sample and of pure melamine show no coincidences. This proves that the reaction product is free from unreacted, recrystallised melamine, which in turn demonstrates the efficiency and selectivity of the procedure.

An additional hint for the actual conversion of melamine can be found in the elemental composition of the sample, in particular the carbon-to-nitrogen ratio. Even though standard energy-dispersive X-ray spectroscopy (EDX) measurements are not reliable enough for precise quantification of elements with low mass, such as carbon and nitrogen,[57,58] the data show that the relative nitrogen content in the sample (C$_{3.0}$N$_{4.6}$) is slightly lower than in the precursor (C$_{3.0}$N$_{6.0}$). Since the polymerisation process is inevitably accompanied by the loss of nitrogen and/or nitrogen-containing species, the EDX measurements qualitatively verify the polymerisation of melamine. More importantly, no other elements, particularly no oxygen, were found in the EDX spectra of the sample (see Fig. S6†), which not only confirms the sample to be pure carbon nitride, but also its stability against oxidation.

Since, as mentioned above, the sensitivity of EDX for light elements is low, we further investigated the sample by means of Fourier-transform infrared (FT-IR) spectroscopy to obtain structural information about the sample and to check for oxygen-containing compounds in the structure. We see that the FT-IR spectrum of the sample, shown in Fig. S7,† is significantly different from the spectrum of pure melamine (e.g. absence of signal 1549 cm^{-1} [59]) and that all signals can accurately be assigned according to the literature. The broad bands at 3319 cm^{-1}, 3118 cm^{-1} and 1599 cm^{-1} correspond to N–H modes,[60,61] while the distinct signals at 2170 cm^{-1} and 2144 cm^{-1} can be assigned to the N=C=N molecular building block.[62–64] Interestingly, these signals are particularly strong, which can be attributed to a certain abundance of this motif in the polymeric network. Finally, the signal at 806 cm^{-1} is assigned to the triazine unit.[65–67] In the FT-IR spectrum, no signals are observed around 1050 cm^{-1}, 1166 cm^{-1} or 1250 cm^{-1} excluding the presence of C–O.[68] There is neither a signal at 1740 cm^{-1} where C=O vibrations would be expected[69] nor at 1350–1530 cm^{-1} for N–O/N=O.[70] The band at 1446 cm^{-1} can be attributed to the C=N stretch vibration mode[71] but is also discussed in the literature to originate from chemisorbed carbon-oxide species.[72,73] Thus, the FT-IR spectrum confirms that the sample consists of pure, most likely

polymeric, carbon nitride. To specify which type of graphitic carbon nitride has been formed, the sample was investigated via photoluminescence (PL) spectroscopy. For this, the covered substrate was irradiated with 403 nm laser light on different spots (theoretical spot size: 215 nm) and emission spectra were recorded, respectively. A representative PL spectrum of the sample is shown in Fig. 3(c). The broad emission signal extends over the entire visible range and shows a maximum at 591 nm, which corresponds to a band gap of 2.1 eV. According to the literature, PTI features a band gap of approx. 3.0 eV[74–76] and HGCN of 2.7–2.9 eV,[56,77–80] while the band gap of TGCN is reported to be much lower at around 2.0 eV.[7,81] Therefore, the PL data give strong evidence that the deposited structure is mainly triazine-based graphitic carbon nitride. The noticeable width of the PL spectrum might be caused by slightly different thicknesses of the TGCN. Considering that single-layer TGCN features a band gap of 2.4 eV,[7] the weakly pronounced shoulder in the PL spectrum at 2.4 eV might indicate the presence of such very thin TGCN structures.

To finally verify that our plasma-based approach leads to TGCN, the sample surface was extensively investigated at the level of chemical bonds by X-ray photoelectron spectroscopy (XPS). The resulting survey spectrum, depicted in Fig. 4(a), shows contribution only from carbon (285 eV), nitrogen (400 eV) and oxygen (530 eV), as well as small amounts of silicon from the substrate (100 eV). The C 1s spectrum in Fig. 4(b) can be deconvoluted into four peaks. These signals correspond to adventitious carbon (adv. C, C–C/C–H, 284.6 eV), a C–NH$_2$ or C–O species (286.6 eV), N–C=N of sp^2-hybridised carbon in the aromatic ring substructure (288.1 eV) and O–C=O (289.2 eV), respectively.[7,82–84] For the N 1s spectrum, shown in Fig. 4(c), two peaks can be identified. The first one at 398.8 eV can be assigned to sp^2-hybridised nitrogen in the aromatic ring
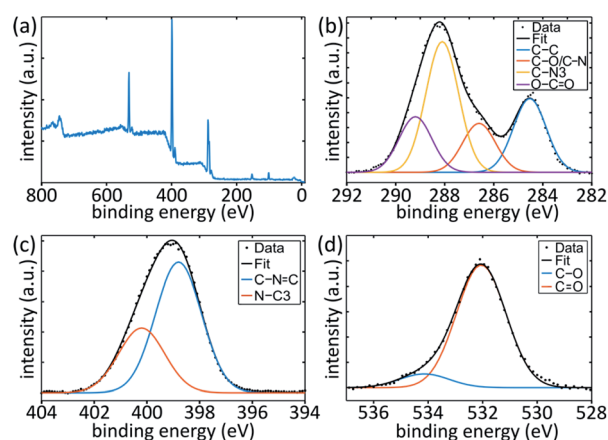

Fig. 4 XPS spectra of a TGCN sample. The survey spectrum (a) shows relevant peaks at 100 eV for Si 2p from the substrate and 285 eV for C 1s, 400 eV for N 1s and 530 eV for O 1s from the sample. The detailed spectra were deconvoluted further and the fits are shown alongside the data. (b) C 1s was fitted with four peaks at 284.6, 286.6, 288.1 and 289.2 eV, for adv. C, C–N/C–O, C–N3 and O–C=O. (c) N 1s with two peaks at 398.8 and 400.2 eV for C–N=C and N–C3 and (d) O 1s also with two peaks at 531.1 and 533.1 eV for C=O and C–O.

9686 | J. Mater. Chem. A, 2022, 10, 9680–9692

This journal is © The Royal Society of Chemistry 2022

(C–N=C) and the latter at 400.2 eV to tertiary nitrogen (N–C3), which forms the bridging part between the ring substructures. Combined with the N–C=N peak from C 1s, these are in good agreement with previous studies on TGCN.[7,83,84] The C 1s peaks for C–C, C–O and O–C=O are commonly associated with adventitious carbon contaminants through air exposure.[82] In a fully condensed system, the expected ratio between the two N 1s peaks is 3 : 1.[7] Here, the ratio is 2 : 1, which indicates that the sample might not be fully condensed. This is not surprising when compared to the SEM data, where a sponge-like structure with a high surface area and a lot of terminating groups can be observed. Difficulties arise in determining the exact degree of condensation, because the C–NH and N–C3 peaks are not unambiguous due to resolution limitations. The former overlaps with oxygen contaminants in C–O and the latter with the N–H2 species.[82,83,85] Fitting the O 1s spectra (Fig. 4(d)) results in two peaks at 531.1 eV for C=O and 533.1 eV for C–O.[82,85] Mild argon sputtering of a sample decreased the amount of oxygen and adventitious carbon with respect to the relevant TGCN peaks, which confirms that most oxygen originates from surface contaminants due to air exposure and is not part of the original structure. The resulting oxygen content is far below the detection limit of the EDX method which is far less surface sensitive than XPS. To clarify the discrepancy between EDX and XPS, we performed elemental analysis of the samples. These data show that the sample consists mainly of nitrogen (65.64%), carbon (28.90%) and hydrogen (4.61%). The rather high nitrogen and hydrogen contents suggest that NH groups are present, which indicates that parts of the deposited film are not fully polymerised. We also conclude from the elemental analysis that the oxygen content can be no more than 0.85%, confirming that oxygen is not present to any significant extent in the structure, but maybe in the form of adsorbates, as it was determined by XPS. In conclusion, these results combined with the other results presented here, confirm the production of highly condensed TGCN.

Influence of plasma parameters

The plasma-induced polymerisation of melamine is a fast and reproducible technique for the deposition of TGCN directly onto solid substrates. Adjustable parameters offer numerous ways to influence the product formation. The substrate temperature, as one parameter, is neglected here since the substrate does not have to be actively heated. Precursor feed is neither investigated further since the precursor flux during the sublimation of a solid precursor compound certainly cannot be controlled and monitored as precisely as with gaseous precursors. Consequently, the crucial adjustment options for the polymer deposition are found in the plasma settings, including input power, chamber pressure, pulsing and modification of electric fields. The main task of the plasma is to generate preferably identical activated monomers that ultimately form a defined polymer by specific recombination. The more unspecific the activation of the monomers and the more arbitrary the fragmentation, the more diverse the recombination possibilities will be, and the more randomly combined

structures might form. According to the literature, a low input power can lead to more regular and better-defined polymers.[86] Hence, a low input power to the plasma of only 10 W was set. In fact, the TGCN deposition is significantly degraded when performing the procedure with an input power of 100 W instead of 10 W. Although significantly more material is deposited at higher power due to the increased ion and electron density, it can be seen from the more yellowish colour and the X-ray diffractogram that the film contains admixtures of other carbon-nitride species than TGCN.

Additionally, to rather activate or fragment the amine substituents of melamine than to decompose the aromatic ring, we intended to keep the mean electron temperature as low as possible by setting a high chamber pressure of 5 mbar. Lowering the chamber pressure from 5 mbar to 1 mbar inhibits any deposition on the substrate. One reason might be that less material reaches the substrate due to the higher flux. Moreover, a lower chamber pressure results in an increase of the average electron temperature. Due to the higher electron energy, much more melamine is completely decomposed in the plasma. The resulting small molecules do not react on the cold substrate surface, so that no product is formed on the substrate.

Pulsing the plasma is a very effective way to further control the energy input into the monomer molecules and to influence the polymer deposition. Radical formation and recombination are temporally separated, i.e., monomer radicals are generated exclusively during the plasma on-state, whereas in the plasma off-state, these radicals form dimeric or oligomeric radicals or are consumed via chain propagation.[87] Each cycle provides newly formed monomer radicals that contribute to the stepwise polymer formation.[86] In fact, we observed a strong effect on the morphology of the deposited product when using continuous plasma instead of pulsed plasma. Although TGCN was obtained in both cases, using continuous plasma resulted in a thin film of TGCN that appears like a foil on the wafer substrate, as can be seen in SEM images (see Fig. S8(a)†). It is noticeable that significantly less product was deposited in the continuous plasma mode, which can also be deduced from the X-ray diffractogram of the sample (see Fig. S8(b)†). Since activation and chain propagation are not temporally separated, the lifetime of activated radicals in continuous plasma is too short to recombine specifically. Instead, fragmentation is dominant resulting in the generation of volatile species that do not contribute to product formation on a cold substrate. Furthermore, the deposition product is permanently exposed to the plasma, which might lead to the removal of the as-deposited material. Thus, continuous plasma allows for the deposition of thin TGCN films, but not for TGCN with a large surface area as required for catalytic purposes. The sponge-like morphology was achieved by pulsing the plasma with a duty cycle of 25%, i.e., a short on-state (5 ms) alternating with a longer off-state (15 ms). Due to the high chamber pressure, and thus short mean free path length, oligomer formation might take place already in the gas phase, leading to a so-called dusty plasma.[88] These structures then merely recombine with the already deposited material on the substrate, which results in the formation of TGCN flakes that constitute the sponge-like morphology of the sample.

This journal is © The Royal Society of Chemistry 2022

J. Mater. Chem. A, 2022, **10**, 9680–9692 | **9687**

Finally, we identified the application of a negative dc bias to the substrate as important for the deposition of pure TGCN. In the literature, constant negative bias is associated with decreased residual stress of hydrogenated amorphous carbon films with nitrogen incorporation.[22,89,90] Here, a superimposed negative voltage was applied to attract the plasma-generated electrophilic radical species and to accelerate them to the substrate for recombination. Electrophilic species are strongly favoured over neutrals, while negatively charged species on the other hand are even rejected. In fact, a negative voltage of −210 V relative to ground enabled much more selective deposition. A control experiment with positive bias showed significant amounts of melamine besides TGCN in the XRD pattern (see Fig. S9†). Without dc bias, hardly any melamine was co-deposited. However, the sample was significantly more mechanically robust when a dc bias of −210 V relative to ground was applied to the substrate, which might be due to a certain bombardment of the substrate with monomer radicals.

Catalytic properties

The overall redox process for light-induced water splitting on the catalyst surface can be divided into two half reactions: (i) the hole-driven oxidation of water into oxygen and protons ($2H_2O + 4h^+ \rightarrow 4H^+ + O_2$, oxygen evolution reaction, OER) and (ii) the electron-driven reduction of protons to molecular hydrogen ($2H^+ + 2e^- \rightarrow H_2$, hydrogen evolution reaction, HER).[91,92]

To enable both the OER and HER reactions with satisfactory efficiency, one crucial property of the photocatalyst is the existence of an adequate band gap (for light harvesting) with appropriate band-edge potentials. Firstly, for efficient photocatalytic water splitting, the band gap of the photocatalyst should ideally be about 2.0–2.2 eV[93,94] with a conduction-band minimum that is more negative than the reduction potential of the proton (−0.41 V vs. NHE, pH 7) and a valence-band maximum that is more positive than the oxidation potential of water (+0.82 V vs. NHE, pH 7).[95] Furthermore, the specific absorbance of the photocatalyst with respect to the solar spectrum for energies above the band gap should be as high as possible. The higher the absorption coefficient the more charge carriers can be generated, which in turn are potentially available for water splitting. Secondly, the charge carrier recombination rate should be negligibly low. The charge carriers need to be effectively separated and transported to the catalyst surface to be available for the redox reactions.[96,97] In general, the surface area plays a decisive role in catalysis, since the interacting surface area between the catalyst and educt is proportional to the efficiency, which is a fundamental key parameter for the quality of any catalyst.[98] In our case, precise physisorption measurements were not feasible since the sample is not powdery and cannot be mechanically removed under preservation of the original film morphology. However, there are several other requirements that should be satisfied. In addition to chemical and mechanical stability, from an economic point of view, a catalyst should be producible in large quantities with low costs. Accordingly, large-scale manufacturing processes and abundant materials are required, or at least favourable, for

catalyst production. Today, most of the commonly used catalysts are based on either rare and/or toxic transition metals, which is also problematic from an ecological perspective.[99–101] TGCN fulfils all the above-mentioned criteria and thus represents a very promising candidate as a photocatalyst for the light-driven production of hydrogen from water. To investigate the photocatalytic activity of the fabricated TGCN, the light-absorption behaviour was investigated first. For this, the TGCN deposition was reproduced with the same reaction parameters as described above, but on a transparent conductive oxide substrate, namely ITO-covered glass. The baseline-corrected UV/Vis spectrum of the sample, depicted in Fig. 5(a), features a maximum of the optical density at 381 nm. At this wavelength the absorptance of the sample is about 99%. Next, a TGCN sample was wetted ex situ with 100 μL D_2O and was transferred into the XPS experimental chamber that was equipped with a sensitive mass spectrometer. Our temperature-programmed desorption (TPD) measurements revealed that residual water is stable on TGCN even under vacuum conditions up to 100–150 °C. This is probably due to the polar nature of TGCN and potentially further enhanced by the sponge-like structure. The mass spectrometer was tuned to 4 amu (mass of D_2) and constantly measured the amount of incoming gas. Then, the D_2 flux was recorded under simultaneous illumination of the sample with LED light with a mean wavelength of 365 nm. The LED was mounted outside the chamber and the illumination took place over 30 min in on/off intervals of 5 min,
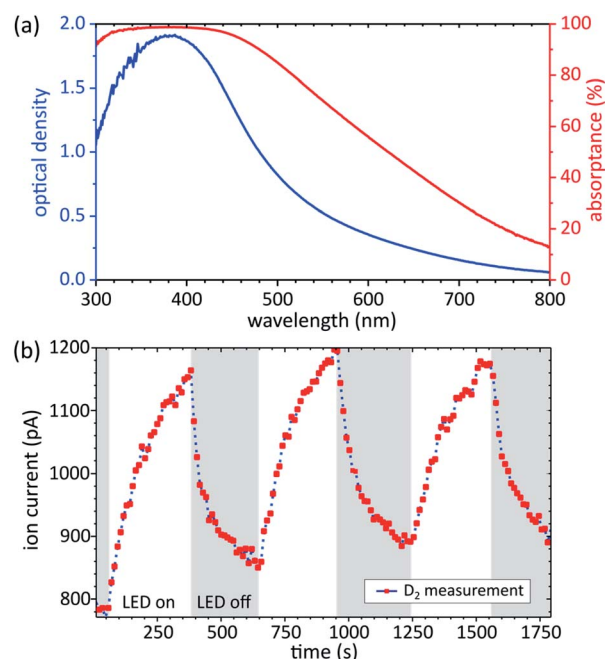

Fig. 5 (a) Absorbance spectrum (blue) and absorptance (red) of a TGCN sample deposited on ITO-covered glass measured with an integrating sphere to consider light scattering. (b) Measurement of deuterium over time in dependence of illumination of a TGCN sample with LED light ($\lambda = 365$ nm) in 5 min on (white)/off (shaded) intervals. The offset in ion current is due to the constant gas pressure on the analyser.

9688 | J. Mater. Chem. A, 2022, 10, 9680–9692

This journal is © The Royal Society of Chemistry 2022

respectively. D_2O was used instead of H_2O, because the D_2 signal can be distinguished from the H_2 signal that might have other origins inside the experimental chamber than the sample. Fig. 5(b) shows the temporal development of the D_2^+ ($m/z = 4$) signal. During the illumination with LED light an increase in the D_2^+ signal can be observed, which returns to initial levels when the LED is turned off. The reliable cyclic production of D_2 from D_2O under light irradiation of the catalyst even after 10 days indicates the recyclability of the produced TGCN films, as already reported in the literature for other graphitic carbon nitrides.[102–104] To verify that the measured D_2 is derived from the photocatalytic reaction on the TGCN surface and not from thermally evaporated D_2O, the sample temperature was monitored. During the experiment, the sample temperature did not change. Moreover, control experiments on bare substrates were performed. Without TGCN no D_2 evolution was detected. This is a strong indication for photocatalytic water splitting and demonstrates the functionality of the deposited nanostructured TGCN. For future prospects, it is of great interest to further tailor the optical and photocatalytic properties of the TGCN by doping, *i.e.*, by inserting cations into the nucleophilic pores of the carbon nitride as has been demonstrated for HGCN.[105–108]

Conclusions

We have presented a novel technique for the rapid and specific deposition of pure crystalline TGCN directly onto wafer substrates and ITO-covered glass slides. For this, solid melamine is used as the monomeric single-source precursor instead of gaseous carbon and nitrogen sources. In a home-built PECVD setup, the substrate is held face-down over a precursor reservoir filled with melamine powder. At 5 mbar chamber pressure, melamine is heated up to 300 °C and is sublimated into a pulsed rf plasma which is surrounding the substrate. The substrate is not actively heated in this process. After 10 min deposition time, a mechanically and thermally very robust film of pure TGCN is formed, which has a silvery-brownish matte appearance. Since melamine serves as a monomer in the plasma-induced polymerisation process, the aromatic solid, which vaporises undecomposed as determined *via* TGA, was characterised in terms of its molecular structure. For this, single-crystal diffraction and binding-energy calculations were performed to identify stable and fragile parts of melamine. It was found that the bonds within the aromatic core are significantly more stable than the bonds of the amine substituents.

In the plasma, decomposition of the molecule then occurs to some extent, which could be deduced from CN signals in the optical emission spectrum *in situ*. However, also mild activation of melamine molecules at the substituents was indicated by distinct NH signals in the emission spectrum of the plasma. The homogeneously coated substrate was investigated in terms of morphology, elemental composition, and structure. Scanning electron microscopy images showed a 4 μm thick layer consisting of two-dimensional nanostructures. The material exhibited hardly any charging effects in the electron beam. Powder X-ray diffraction of the deposited product displayed its crystallinity. Here, only one reflection at 27.1° occurs that can be assigned to

the (002) reflection originating from the stacking of the graphitic layers. The assignment of the product and its identification as TGCN were also enabled by photoluminescence spectroscopy. The PL spectrum featured one broad emission signal with a maximum at 591 nm, which corresponds to a band gap of 2.1 eV. This value is characteristic for TGCN and allows for exclusion of melon, PTI or HGCN, since these carbon nitrides feature much higher band gaps of approx. 3 eV. The deposition of pure TGCN was also confirmed by detailed XPS studies. We found that constant biasing of the substrate with −210 V relative to ground gains selectivity and inhibits the co-deposition of melamine. We showed that plasma pulsing strongly influences the morphology of the deposition product and identified short pulses of 5 ms with long plasma off-states (15 ms) to be crucial for nanostructuring of the TGCN. Finally, the photocatalytic activity of the deposited TGCN was investigated by performing overall water-splitting experiments with D_2O. Illumination of the D_2O-wetted TGCN with UV light instantaneously led to the production of D_2, which was measured *via* mass spectrometry. On/off cycling of the illumination allows for correlating the formation of D_2 with the photocatalytic activity of the TGCN sample.

Our novel plasma-induced polymerisation procedure allows for the fast and reproducible fabrication of high-quality TGCN coatings directly on substrates. The unique combination of using easy-to-handle low-cost melamine powder as the precursor, the application of a cold rf plasma as the reaction medium and the very short process duration time makes the approach particularly sustainable compared to other methods. Since micrometre thick nanostructured films are generated within minutes, this technique offers high-throughput fabrication of TGCN and, also due to the gas-based chemistry, represents an industrially scalable approach for controlled TGCN deposition. Thus, the presented technique finally enables effective utilisation of the material for numerous photocatalytic purposes and significantly contributes to the future application of organic semiconductors in photochemical devices.

Conflicts of interest

There are no conflicts to declare.

Acknowledgements

Notes and references

1 G. Nicoletti, N. Arcuri, G. Nicoletti and R. Bruno, *Energy Convers. Manage.*, 2015, **89**, 205–213.
2 C. Tarhan and M. A. Çil, *J. Energy Storage*, 2021, **40**, 102676.

This journal is © The Royal Society of Chemistry 2022

J. Mater. Chem. A, 2022, **10**, 9680–9692 | **9689**

3   Y. Wang, X. Wang and M. Antonietti, *Angew. Chem., Int. Ed.*, 2012, **51**, 68–89.

4   A. Wang, C. Wang, L. Fu, W. Wong-Ng and Y. Lan, *Nano-Micro Lett.*, 2017, **9**, 47.

5   Y. Zheng, L. Lin, B. Wang and X. Wang, *Angew. Chem., Int. Ed.*, 2015, **54**, 12868–12884.

6   X. Wang, S. Blechert and M. Antonietti, *ACS Catal.*, 2012, **2**, 1596–1606.

7   G. Algara-Siller, N. Severin, S. Y. Chong, T. Björkman, R. G. Palgrave, A. Laybourn, M. Antonietti, Y. Z. Khimyak, A. V. Krasheninnikov, J. P. Rabe, U. Kaiser, A. I. Cooper, A. Thomas and M. J. Bojdys, *Angew. Chem., Int. Ed.*, 2014, **53**, 7450–7455.

8   W. K. Darkwah and Y. Ao, *Nanoscale Res. Lett.*, 2018, **13**, 388.

9   B. Zhu, B. Cheng, L. Zhang and J. Yu, *Carbon Energy*, 2019, **1**, 32–56.

10 D. M. Teter and R. J. Hemley, *Science*, 1996, **271**, 53–55.

11 A. M. Silva and M. I. Rojas, *Comput. Theor. Chem.*, 2016, **1098**, 41–49.

12 T. Suter, V. Brázdová, K. McColl, T. S. Miller, H. Nagashima, E. Salvadori, A. Sella, C. A. Howard, C. W. M. Kay, F. Corà and P. F. McMillan, *J. Phys. Chem. C*, 2018, **122**, 25183–25194.

13 T. S. Miller, A. B. Jorge, T. M. Suter, A. Sella, F. Corà and P. F. McMillan, *Phys. Chem. Chem. Phys.*, 2017, **19**, 15613–15638.

14 Q. Guo, Y. Xie, X. Wang, S. Lv, T. Hou and X. Liu, *Chem. Phys. Lett.*, 2003, **380**, 84–87.

15 Q. Guo, Y. Xie, X. Wang, S. Zhang, T. Hou and S. Lv, *Chem. Commun.*, 2004, 26–27.

16 J. Li, C. Cao, J. Hao, H. Qiu, Y. Xu and H. Zhu, *Diamond Relat. Mater.*, 2006, **15**, 1593–1600.

17 J. Li, C. Cao and H. Zhu, *Nanotechnology*, 2007, **18**, 115605.

18 E. Kroke, M. Schwarz, E. Horath-Bordon, P. Kroll, B. Noll and A. D. Norman, *New J. Chem.*, 2002, **26**, 508–512.

19 Y. Noda, C. Merschjann, J. Tarábek, P. Amsalem, N. Koch and M. J. Bojdys, *Angew. Chem., Int. Ed.*, 2019, **58**, 9394–9398.

20 J. Kouvetakis, M. Todd, B. Wilkens, A. Bandari and N. Cave, *Chem. Mater.*, 1994, **6**, 811–814.

21 Y. Wang, F. Wang, Y. Zuo, X. Zhang and L.-F. Cui, *Mater. Lett.*, 2014, **136**, 271–273.

22 D. F. Franceschini and F. L. Freire, *Diamond Relat. Mater.*, 1996, **5**, 471–474.

23 E. F. Motta and I. Pereyra, *J. Non-Cryst. Solids*, 2004, **338**, 525–529.

24 N. H. Khanis, R. Ritikos, M. Othman, N. M. Abdul Rashid, S. M. A. Gani and S. A. Rahman, *Mater. Chem. Phys.*, 2013, **138**, 514–518.

25 N. Khanis, R. Ritikos, S. Ahmad Kamal and S. Abdul Rahman, *Materials*, 2017, **10**, 102.

26 M. J. Frisch, G. W. Trucks, H. B. Schlegel, G. E. Scuseria, M. A. Robb, J. R. Cheeseman, G. Scalmani, V. Barone, G. A. Petersson, H. Nakatsuji, X. Li, M. Caricato, A. Marenich, J. Bloino, B. G. Janesko, R. Gomperts, B. Mennucci, H. P. Hratchian, J. V. Ortiz, A. F. Izmaylov, J. L. Sonnenberg, D. Williams-Young, F. Ding, F. Lipparini, F. Egidi, J. Goings, B. Peng, A. Petrone, T. Henderson, D. Ranasinghe, V. G. Zakrzewski, J. Gao, N. Rega, G. Zheng, W. Liang, M. Hada, M. Ehara, K. Toyota, R. Fukuda, J. Hasegawa, M. Ishida, T. Nakajima, Y. Honda, O. Kitao, H. Nakai, T. Vreven, K. Throssell, J. A. Montgomery Jr, J. E. Peralta, F. Ogliaro, M. Bearpark, J. J. Heyd, E. Brothers, K. N. Kudin, V. N. Staroverov, T. Keith, R. Kobayashi, J. Normand, K. Raghavachari, A. Rendell, J. C. Burant, S. S. Iyengar, J. Tomasi, M. Cossi, J. M. Millam, M. Klene, C. Adamo, R. Cammi, J. W. Ochterski, R. L. Martin, K. Morokuma, O. Farkas, J. B. Foresman and D. J. Fox, *Gaussian 09*, Gaussian, Inc., Wallingford, CT, 2016.

27 C. Ruhmlieb, Y. J. Lee, C. Strelow, T. Kipp and A. Mews, *J. Mater. Chem. C*, 2019, **7**, 10098–10110.

28 C. Wang, R. Pagel, D. W. Bahnemann and J. K. Dohrmann, *J. Phys. Chem. B*, 2004, **108**, 14082–14092.

29 C. Duan, D. Yuan, Z. Yang, S. Li, L. Tao, Q. Wang and T. Wang, *Composites, Part A*, 2018, **113**, 200–208.

30 L. Costa and G. Camino, *J. Therm. Anal.*, 1988, **34**, 423–429.

31 S. Chaitoglou, E. Pascual, E. Bertran and J. L. Andujar, *J. Nanomater.*, 2016, **2016**, 54–64.

32 P. Lamichhane, B. Ghimire, S. Mumtaz, R. Paneru, S. H. Ki and E. H. Choi, *J. Phys. D: Appl. Phys.*, 2019, **52**, 265206.

33 D. Zhang, Q. Gao, B. Li, J. Liu and Z. Li, *Appl. Opt.*, 2019, **58**, 1210–1214.

34 A. Fateev, F. Leipold, Y. Kusano, B. Stenum, E. Tsakadze and H. Bindslev, *Plasma Processes Polym.*, 2005, **2**, 193–200.

35 M. F. J. Vos, G. van Straaten, W. M. M. E. Kessels and A. J. M. Mackus, *J. Phys. Chem. C*, 2018, **122**, 22519–22529.

36 E. G. Wang, Z. G. Guo, J. Ma, M. M. Zhou, Y. K. Pu, S. Liu, G. Y. Zhang and D. Y. Zhong, *Carbon*, 2003, **41**, 1827–1831.

37 G. Panomsuwan, S. Chiba, Y. Kaneko, N. Saito and T. Ishizaki, *J. Mater. Chem. A*, 2014, **2**, 18677–18686.

38 D. Tsyganov, N. Bundaleska, A. Dias, J. Henriques, E. Felizardo, M. Abrashev, J. Kissovski, A. M. B. do Rego, A. M. Ferraria and E. Tatarova, *Phys. Chem. Chem. Phys.*, 2020, **22**, 4772–4787.

39 R. L. Vander Wal, C. K. Gaddam and M. J. Kulis, *J. Anal. Spectrom.*, 2014, **29**, 1791–1798.

40 T. J. Wasowicz, A. Kivimäki, M. Coreno and M. Zubek, *J. Phys. B: At., Mol. Opt. Phys.*, 2014, **47**, 055103.

41 X. He, M. Zheng, J. Qiu, Z. Zhao and T. Ma, *Plasma Sources Sci. Technol.*, 2006, **15**, 246–252.

42 Y. Yamagata, A. Sharma, J. Narayan, R. M. Mayo, J. W. Newman and K. Ebihara, *J. Appl. Phys.*, 2000, **88**, 6861–6867.

43 P. Jamroz and W. Zyrnicki, *Eur. Phys. J.: Appl. Phys.*, 2002, **19**, 201–209.

44 L. Souqui, J. Palisaitis, H. Högberg and H. Pedersen, *J. Mater. Chem. C*, 2020, **8**, 4112–4123.

45 X.-M. Zhu, W.-C. Chen, J. Li and Y.-K. Pu, *J. Phys. Appl. Phys.*, 2009, **42**, 025203.

46 F. J. Gordillo-Vázquez, M. Camero and C. Gómez-Aleixandre, *Plasma Sources Sci. Technol.*, 2006, **15**, 42–51.

47 A. Bousetta, M. Lu, A. Bensaoula and A. Schultz, *Appl. Phys. Lett.*, 1994, **65**, 696–698.

9690 | *J. Mater. Chem. A*, 2022, **10**, 9680–9692

This journal is © The Royal Society of Chemistry 2022

48 S. Zheng, G. Zhong, X. Wu, L. D'Arsiè and J. Robertson, *RSC Adv.*, 2017, **7**, 33185–33193.

49 A. G. Gaydon and R. W. B. Pearse, *The Identification of Molecular Spectra*, Springer, Netherlands, 1976.

50 Y. Cui, J. Zhang, G. Zhang, J. Huang, P. Liu, M. Antonietti and X. Wang, *J. Mater. Chem.*, 2011, **21**, 13032–13039.

51 P. Sharma and Y. Sasson, *Green Chem.*, 2017, **19**, 844–852.

52 J.-Y. Kang, W. Ha, H.-X. Zhang and Y.-P. Shi, *Microchim. Acta*, 2020, **187**, 76.

53 J. Wu, C. M. Shaw and D. C. Martin, in *Polymer Science: A Comprehensive Reference*, ed. M. Moeller and K. Matyjaszewski, Elsevier Science & Technology, Oxford, United Kingdom, 2nd edn, 2012, ch. 2.19.

54 F. Fina, S. K. Callear, G. M. Carins and J. T. S. Irvine, *Chem. Mater.*, 2015, **27**, 2612–2618.

55 A. Thomas, A. Fischer, F. Goettmann, M. Antonietti, J.-O. Müller, R. Schlögl and J. M. Carlsson, *J. Mater. Chem.*, 2008, **18**, 4893–4908.

56 Q. Liang, Z. Li, Z.-H. Huang, F. Kang and Q.-H. Yang, *Adv. Funct. Mater.*, 2015, **25**, 6885–6892.

57 C.-U. Ro, J. Osán and R. Van Grieken, *Anal. Chem.*, 1999, **71**, 1521–1528.

58 M. F. Gazulla, M. Rodrigo, E. Blasco and M. Orduña, *X-Ray Spectrom.*, 2013, **42**, 394–401.

59 X. Yuan, K. Luo, K. Zhang, J. He, Y. Zhao and D. Yu, *J. Phys. Chem. A*, 2016, **120**, 7427–7433.

60 Y. Zhao, D. Yu, H. Zhou and Y. Tian, *J. Mater. Sci.*, 2005, **40**, 2645–2647.

61 T. Chhabra, A. Bahuguna, S. Singh Dhankhar, C. M. Nagaraja and V. Krishnan, *Green Chem.*, 2019, **21**, 6012–6026.

62 Y.-L. Li, E. Kroke, A. Klonczynski and R. Riedel, *Adv. Mater.*, 2000, **12**, 956–961.

63 H. Chenga, Y. Li, E. Kroke and S. Herkenhoff, *J. Eur. Ceram. Soc.*, 2013, **33**, 2181–2189.

64 D. Zhang, T. Xu, C. Li, W. Xu, J. Wang and J. Bai, *J. CO$_2$ Util.*, 2019, **34**, 716–724.

65 H. Zou, X. Yan, J. Ren, X. Wu, Y. Dai, D. Sha, J. Pan and J. Liu, *Journal of Materiomics*, 2015, **1**, 340–347.

66 S. K. Kundu and A. Bhaumik, *RSC Adv.*, 2015, **5**, 32730–32739.

67 W. Gao, Y. Zhao, Z. Mao, D. Bi, J. Chen and D. Wang, *J. Mater. Sci.*, 2018, **53**, 9473–9485.

68 F. Dong, Y. Li, Z. Wang and W.-K. Ho, *Appl. Surf. Sci.*, 2015, **358**, 393–403.

69 J. Wang, Z. Li, S. Li, W. Qi, P. Liu and F. Liu, *PLoS One*, 2013, **8**, e72475.

70 M. Ak, B. Gacal, B. Kiskan, Y. Yagci and L. Toppare, *Polymer*, 2008, **49**, 2202–2210.

71 J. Hao, X. Gao, Y. Jiang, F. Xie, Z. Shao and B. Yi, *RSC Adv.*, 2017, **7**, 52812–52821.

72 N. Sutradhar, A. Sinhamahapatra, S. Kumar Pahari, P. Pal, H. C. Bajaj, I. Mukhopadhyay and A. Baran Panda, *J. Phys. Chem. C*, 2011, **115**, 12308–12316.

73 N. K. Nga, N. T. T. Chau and P. H. Viet, *J. Sci.: Adv. Mater. Devices*, 2020, **5**, 65–72.

74 L. Heymann, B. Schiller, H. Noei, A. Stierle and C. Klinke, *ACS Omega*, 2018, **3**, 3892–3900.

75 Y. Ham, K. Maeda, D. Cha, K. Takanabe and K. Domen, *Chem. – Asian J.*, 2013, **8**, 218–224.

76 Y. Zhang, L. Hu, C. Zhu, J. Liu, H. Huang, Y. Liu and Z. Kang, *Catal. Sci. Technol.*, 2016, **6**, 7252–7258.

77 D. Zhang, W. He, J. Ye, X. Gao, D. Wang and J. Song, *Small*, 2021, **17**, 2005149.

78 Y. Yang, S. Wang, Y. Li, J. Wang and L. Wang, *Chem. – Asian J.*, 2017, **12**, 1421–1434.

79 B. Luo, G. Liu and L. Wang, *Nanoscale*, 2016, **8**, 6904–6920.

80 B. Luo, Y. Zhao and D. Jing, *Front. Energy*, 2021, **15**, 600–620.

81 D. Vidyasagar, T. Bhoyar, G. Singh and A. Vinu, *Macromol. Rapid Commun.*, 2021, **42**, 2000676.

82 G. Greczynski and L. Hultman, *Prog. Mater. Sci.*, 2020, **107**, 100591.

83 S. Dyjak, W. Kiciński and A. Huczko, *J. Mater. Chem. A*, 2015, **3**, 9621–9631.

84 J. Fang, H. Fan, M. Li and C. Long, *J. Mater. Chem. A*, 2015, **3**, 13819–13826.

85 J. Ederer, P. Janoš, P. Ecorchard, J. Tolasz, V. Štengl, H. Beneš, M. Perchacz and O. Pop-Georgievski, *RSC Adv.*, 2017, **7**, 12464–12473.

86 J. Friedrich, *Plasma Processes Polym.*, 2011, **8**, 783–802.

87 H. Yasuda and T. Hsu, *J. Polym. Sci., Polym. Chem. Ed.*, 1977, **15**, 81–97.

88 R. Merlino, *Adv. Phys.: X*, 2021, **6**, 1873859.

89 N. Dwivedi, S. Kumar, H. K. Malik, C. M. S. Rauthan and O. S. Panwar, *Mater. Chem. Phys.*, 2011, **130**, 775–785.

90 N. Dwivedi, S. Kumar and H. K. Malik, *J. Appl. Phys.*, 2012, **111**, 014908.

91 T. Kawawaki, M. Kawachi, D. Yazaki, Y. Akinaga, D. Hirayama and Y. Negishi, *Nanomaterials*, 2022, **12**, 344.

92 H. Chand, A. Kumar and V. Krishnan, *Adv. Mater. Interfaces*, 2021, **8**, 2100045.

93 J. R. Bolton, *Sol. Energy*, 1996, **57**, 37–50.

94 R. M. Navarro Yerga, M. C. Álvarez Galván, F. del Valle, J. A. Villoria de la Mano and J. L. G. Fierro, *ChemSusChem*, 2009, **2**, 471–485.

95 N. Fajrina and M. Tahir, *Int. J. Hydrogen Energy*, 2019, **44**, 540–577.

96 A. Kumar, A. Kumar and V. Krishnan, *ACS Catal.*, 2020, **10**, 10253–10315.

97 A. Kumar, M. Kumar, V. N. Rao, M. V. Shankar, S. Bhattacharya and V. Krishnan, *J. Mater. Chem. A*, 2021, **9**, 17006–17018.

98 X. Li, J. Yu and M. Jaroniec, *Chem. Soc. Rev.*, 2016, **45**, 2603–2636.

99 N. Kaur and D. Kishore, *Catal. Surv. Asia*, 2013, **17**, 20–42.

100 K. Morgan, A. Goguet and C. Hardacre, *ACS Catal.*, 2015, **5**, 3430–3445.

101 K. S. Egorova and V. P. Ananikov, *Organometallics*, 2017, **36**, 4071–4090.

102 J. Guo, Y. Wang, Y. Li, K. Lu, S. Liu, W. Wang and Y. Zhang, *Adv. Synth. Catal.*, 2020, **362**, 3898–3904.

This journal is © The Royal Society of Chemistry 2022

J. Mater. Chem. A, 2022, **10**, 9680–9692 | **9691**

103 H. Ghafuri, Z. Tajik, N. Ghanbari and P. Hanifehnejad, *Sci. Rep.*, 2021, **11**, 19792.

104 X. Fu, Y. Si, L. Qiao, Y. Zhao, X. Chen and B. Yua, *Adv. Synth. Catal.*, 2022, **364**, 574–580.

105 L. Ai, R. Shi, J. Yang, K. Zhang, T. Zhang and S. Lu, *Small*, 2021, **17**, 2007523.

106 S.-F. Ng, J. J. Foo and W.-J. Ong, *InfoMat*, 2022, **4**, e12279.

107 X. Yu, S.-F. Ng, L. K. Putri, L.-L. Tan, A. R. Mohamed and W.-J. Ong, *Small*, 2021, **17**, 2006851.

108 Q. Zhu, Z. Xu, B. Qiu, M. Xing and J. Zhang, *Small*, 2021, **17**, 2101070.

9692 | *J. Mater. Chem. A*, 2022, **10**, 9680–9692

This journal is © The Royal Society of Chemistry 2022